



RETROFIT SOLUTIONS TO ACHIEVE 55% GHG REDUCTION BY 2030

Report on the numerical simulation of WASP effect

WP 4 – Wind Assisted Propulsion
Task 4.5 – Numerical simulation of WASP effect
D4.8 – Report on the numerical simulation of WASP effect
Partners involved: NTUA, AWS, CNR, FSYS, LJMU, AES
Authors: Manolis Angelou (NTUA), George Papadakis (NTUA)





Project details

Project Title	RETROFIT SOLUTIONS TO ACHIEVE 55% GHG REDUCTION BY 2030
Project Type	Innovation Action
Project Acronym	RETROFIT55
Grant Agreement No.	101096068
Duration	36 M
Project Start Date	01/01/2023

Deliverable information

Status (F: final; D: draft; RD: revised draft)	F 03/06/2025
Planned delivery date	31/12/2024
Actual delivery date	03/06/2025
<ul style="list-style-type: none"> • Dissemination level: PU – Public, fully open, e.g. web (Deliverables flagged as public will be automatically published in CORDIS project’s page) • SEN – Sensitive, limited under the conditions of the Grant Agreement • Classified R-UE/EU-R – EU RESTRICTED under the Commission Decision No2015/444 • Classified C-UE/EU-C – EU CONFIDENTIAL under the Commission Decision No2015/444 <p>Classified S-UE/EU-S – EU SECRET under the Commission Decision No2015/444</p>	
Type: Report, Website, Other, Ethics	Report





Document history

Version	Date	Created/Amended by	Changes
1	30/04/2025	Manolis Angelou	First Draft
2	19/05/2025	Mingyang Zhang	Technical revision
3	21/05/2025	Emanuele Spinosa	Technical and editorial revision
Final	27/05/2025	Manolis Angelou	Revision

Quality check review

Reviewer (s)	Main changes / Actions
Mingyang Zhang (AALTO)	Technical revision
Emanuele Spinosa (CNR)	Technical and editorial revision
Cecilia Leotardi (CNR)	Final editorial revision
Cecilia Leotardi and Alessandro Iafra(CNR)	Final review of contents and submission to EC.





Table of Contents

List of figures5
List of tables.....7
List of abbreviations.....8
Executive summary.....9
1 Introduction11
2 Numerical modelling13
2.1 Calculation of apparent wind.....14
2.2 Potential flow BEM in 3D16
2.3 Viscous flow in 2D and recreation of forces on wing surface19
2.4.1 Uniform wind flow23
2.4.2 Boundary layer profile24
3 Closing remarks26
References27
Appendix A – Lift and Drag Coefficients and Vertical centre of effort for each configuration and uniform inflow angle28



List of figures

Figure 1: Sample configurations Wing Sail. Left : Case 13 (Rotation 30° , Twist 10°), Case 20 (Rotation 35° , Twist 25°), Case 27 (Rotation 45° , Twist 20°). Right : Dimensions of Case 1 (Rotation 0° , Twist 0°).....	12
Figure 2: Flowchart of aerodynamics calculations process.....	13
Figure 3: Root and tip chord sections, mast rotation (green arrow) and difference in twist (purple arrow).	14
Figure 4: Apparent wind twist (left); Definition sketch of trim angle (random presented values of 0° , 20° and 40° trim) (right).....	14
Figure 5: True and apparent wind velocity magnitude and angle. (Uniform true wind of 10.0 m/s, wing-sail velocity of 6.5 m/s, true wind angle of 30° . Occurring apparent wind velocity magnitude equal to 15.96 m/s and apparent wind angle equal to 18.2°).....	15
Figure 6: True and apparent wind velocity magnitude and angle. True wind dictated by Profile Power Law.....	16
Figure 7: Discretized geometry with the cosine spacing scheme. Configuration no. 10.....	17
Figure 8: Wind angles (true, apparent, and effective). Configuration no. 10.	19
Figure 9: Equidistant (per 2.5 m) horizontal sections. Configuration no. 10.	20
Figure 10: Configuration no. 10. Section 5 ($z = 10.0\text{ m}$). Sample pressure distributions. At 20° incidence separation near the trailing edge appears (horizontal curve beyond $x/c=0.7$), at 35° incidence the separation point has moved forward (horizontal curve beyond $x/c=0.2$), while at 50° incidence full leading edge separation has occurred.	22
Figure 11: Force coefficients for wing-wail configuration 22.	23
Figure 12: Force coefficients for wing-sail configuration 22. Uniform and power-law profiles.....	24
Figure 13: Force coefficients for wing-sail configuration 22. Uniform flow. Coupled solver and MaPFlow.....	25
Figure 14: Force coefficients (top) and vertical center of effort (bottom). Configuration 1.....	28
Figure 15: Force coefficients (top) and vertical center of effort (bottom). Configuration 2.....	28
Figure 16: Force coefficients (top) and vertical center of effort (bottom). Configuration 3.....	29
Figure 17: Force coefficients (top) and vertical center of effort (bottom). Configuration 4.....	29
Figure 18: Force coefficients (top) and vertical center of effort (bottom). Configuration 5.....	30
Figure 19: Force coefficients (top) and vertical center of effort (bottom). Configuration 6.....	30
Figure 20: Force coefficients (top) and vertical center of effort (bottom). Configuration 7.....	31
Figure 21: Force coefficients (top) and vertical center of effort (bottom). Configuration 8.....	31
Figure 22: Force coefficients (top) and vertical center of effort (bottom). Configuration 9.....	32
Figure 23: Force coefficients (top) and vertical center of effort (bottom). Configuration 10.....	32
Figure 24: Force coefficients (top) and vertical center of effort (bottom). Configuration 11.....	33
Figure 25: Force coefficients (top) and vertical center of effort (bottom). Configuration 12.....	33
Figure 26: Force coefficients (top) and vertical center of effort (bottom). Configuration 13.....	34
Figure 27: Force coefficients (top) and vertical center of effort (bottom). Configuration 14.....	34
Figure 28: Force coefficients (top) and vertical center of effort (bottom). Configuration 15.....	35
Figure 29: Force coefficients (top) and vertical center of effort (bottom). Configuration 16.....	35
Figure 30: Force coefficients (top) and vertical center of effort (bottom). Configuration 17.....	36
Figure 31: Force coefficients (top) and vertical center of effort (bottom). Configuration 18.....	36
Figure 32: Force coefficients (top) and vertical center of effort (bottom). Configuration 19.....	37
Figure 33: Force coefficients (top) and vertical center of effort (bottom). Configuration 20.....	37
Figure 34: Force coefficients (top) and vertical center of effort (bottom). Configuration 21.....	38



Figure 35: Force coefficients (top) and vertical center of effort (bottom). Configuration 22.	38
Figure 36: Force coefficients (top) and vertical center of effort (bottom). Configuration 23.	39
Figure 37: Force coefficients (top) and vertical center of effort (bottom). Configuration 24.	39
Figure 38: Force coefficients (top) and vertical center of effort (bottom). Configuration 25.	40
Figure 39: Force coefficients (top) and vertical center of effort (bottom). Configuration 26.	40
Figure 40: Force coefficients (top) and vertical center of effort (bottom). Configuration 27.	41
Figure 41: Force coefficients (top) and vertical center of effort (bottom). Configuration 28.	41





List of tables

Table 1: Geometrical parameters of Wing Sail cases	11
Table 2: Force coefficients for wing-eail configuration 22.	23





List of abbreviations

2D-3D	Two or Three Dimensional
AWS	Advanced Wing Systems
BEM	Boundary Elements Method
ESD	Energy Saving Device
VCE	Vertical Centre of Effort
WASP	Wind Assisted Ship Propulsion



Executive summary

This report aims to numerically assess the aerodynamic performance of several WASP (Wind Assisted Ship Propulsion) configurations, as they are developed by ADVANCED WING SYSTEMS (AWS), under uniform (or non-uniform) wind flow conditions. These configurations are all possible geometric shapes of a stowable and containerised device that can be placed on a vessel's deck in various numbers and positional arrangements. The key functionality of the systems resides in the capability it offers to the operator to reshape the wing geometry by altering certain geometric parameters (mast rotation and topmost sections twist). This allows the creation of different wing configurations that can take advantage of the wind conditions while the vessel is under way. The adjustments on these configurations can be continuous. For this study we examine a provided group of 28 geometries, which is considered a representative subset of possible configurations.

In terms of the exciting wind, the operation of WASP devices on a vessel involves non-uniform inflow distributions and complex aerodynamic phenomena. In fact, the wind velocity profile clearly exhibits the characteristics of a boundary layer, relative to a horizontal surface such as land, sea, or a ship's deck, depending on the ship's position and the location of the wing-sail. This affects the inflow to an investigated body, an inflow which is also affected in terms of magnitude and angle not only because the ship is moving but also because the WASP device is not limited to a single trimmed condition. In general, to trim a WASP device means to make adjustments to it, either by reshaping it or more often by simply rotating it with respect to the wind. Thus in the case of small changes in the incident wind angle, the optimum performance of the device is achieved by adjusting the trim settings accordingly. Moreover, in cases where the inflow angle is considerable large and flow separation persists, trimming is necessary to negate this prohibiting factor for the performance of the WASP device by altering its settings to a different operational profile. In the context of this report, and as each configuration is evaluated as a stand-alone geometry, the latter definition of trim is meant exclusively, i.e. to trim is to rotate the device along its vertical axis.

From the above considerations, it is clear that there are numerous possible combinations of wind profiles, configurations and wing-sail trim settings, making computationally infeasible to exhaustively analyse all parameter combinations.

Therefore, the report addresses mainly the simplified case of wind velocity uniform in the vertical direction for the AWS Wing-Sail configurations and allows for the computation of lift and drag coefficients. For representative reasons the report includes also a scenario with the wind defined by a non-uniform vertical profile.

The computational tool that was used for the above consists of a coupled 3D potential flow – 2D inviscid/viscous flow numerical scheme. Comparisons with a 3D CFD in-house solver are also presented.

The structure of the report is as follows: after a short introduction on the Wing-Sail configurations, the implemented numerical solution methods are presented. Initially with the calculations for the wind vertical profile (uniform or gradual) and the apparent wind characteristics. The following section regards the 3D Boundary Element Method (BEM) in potential flow for the calculation of downwash velocity. Next, the pre-calculations of 2D pressure coefficient distributions using a viscous-inviscid scheme are discussed as well as the association of these distributions with the 3D effects and the effective angle of attack (via the downwash velocity). Following this, the transformation of the pressure data to forces and force coefficients is presented. Sampled calculated force coefficients



are presented for the cases of both uniform and non-uniform wind. A verification case using a 3D CFD solver is also presented. After the conclusion section, Appendix A contains the figure-data of the lift and drag coefficients and the vertical centre of effort for the provided configurations subjected to uniform flow. The present analysis will support the development of the surrogate model in WP1 and of the weather routing model in WP7.



1 Introduction

The future of worldwide shipping is being planned with increased interest in environmental protection. This is evident in the form of new international rules and regulations aimed at reducing greenhouse gases (and fuel consumption), with the target requiring a decrease of at least 55% by 2030 [1]. Compliance with this is achieved by incorporating more efficient operational practices (e.g., weather routing) or the implementation of new technologies, such as Energy Saving Devices (ESD), which may increase the hull and propeller performance. In addition, wind energy can be harnessed by the installation of Wind Assisted Ship Propulsion (WASP) systems. This report focuses on the numerical modelling of the fluid performance of a WASP (Wing Sail Power) device, which is being developed by one of the project partners, Advanced Wing Systems (AWS).

1.1 Wing Sail of ADVANCED WING SYSTEMS

The AWS wing-sail system is a stowable, containerised unit that can be deployed on a vessel's deck in various numbers and configurations. In terms of fluid dynamics, the key functionality of the systems resides in the capability it offers the operator to reshape the wing geometry by altering certain geometric parameters. These include firstly the mast rotation, that causes an offset sliding motion of the pressure and suction sides, and secondly a twist of the topmost sections. This allows the creation of different wing configurations that can take advantage of the wind conditions encountered while the vessel is under way. The current family of different configurations (cases), 28 in number, is characterized by the geometrical parameters listed in Table 1. A few sample cases are presented in Figure 1 (and the principal dimensions are fixed only in terms of this specific design subset. For other designs beyond this report, parameters such as mast height and aspect ratio may be different. Also, maximum attainable twist angles can be greater than 25°). Apart from the aforementioned parameters, the whole device may also be trimmed, i.e. rotated (Figure 4, right).

Table 1: Geometrical parameters of Wing Sail cases

Case	Rotation (°)	Twist (°)	Case	Rotation (°)	Twist (°)
1	0	0	15	30	20
2	5	5	16	30	25
3	10	10	17	35	10
4	15	10	18	35	15
5	15	15	19	35	20
6	20	10	20	35	25
7	20	15	21	40	10
8	20	20	22	40	15
9	25	10	23	40	20
10	25	15	24	40	25
11	25	20	25	45	10
12	25	25	26	45	15
13	30	10	27	45	20
14	30	15	28	45	25

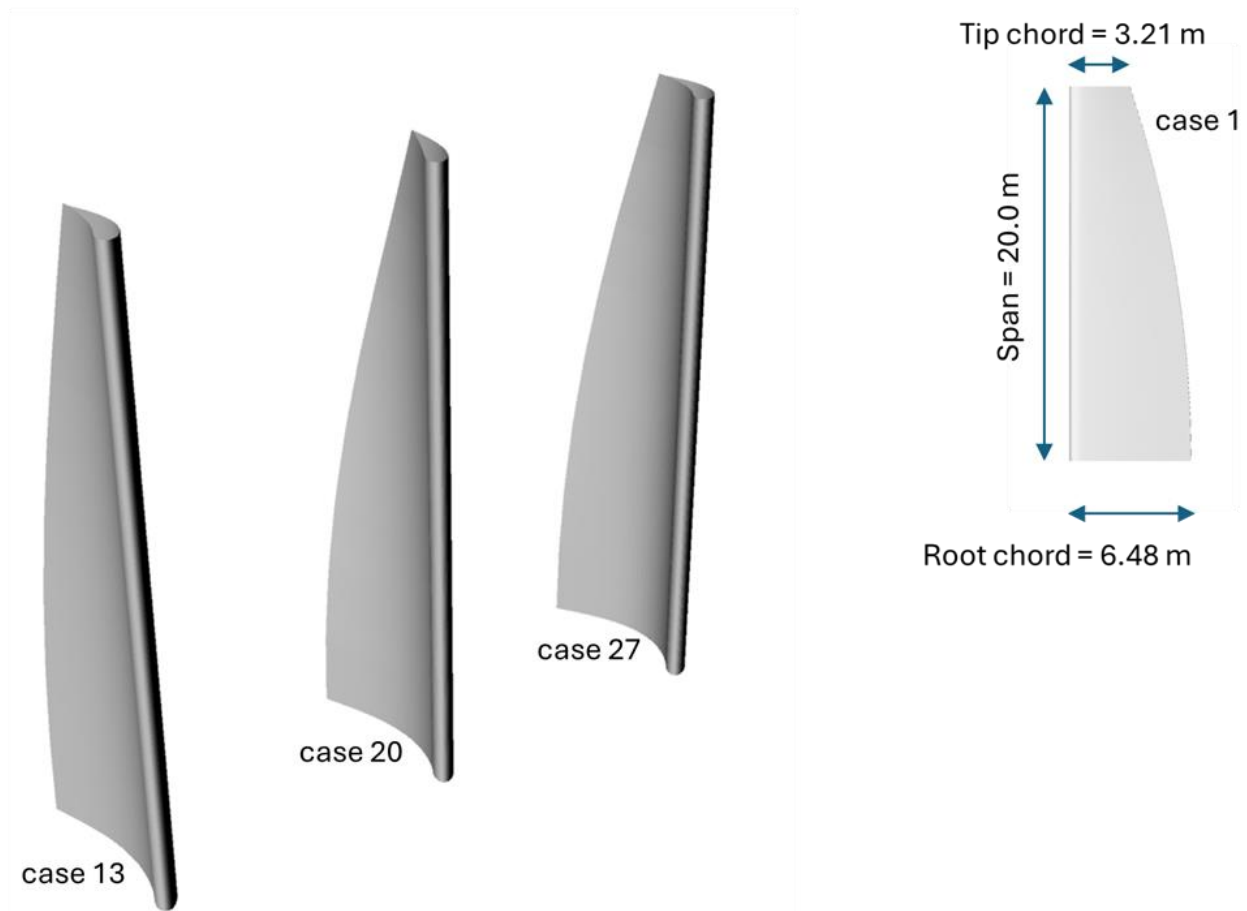


Figure 1: Sample configurations Wing Sail. Left : Case 13 (Rotation 30°, Twist 10°), Case 20 (Rotation 35°, Twist 25°), Case 27 (Rotation 45°, Twist 20°). Right : Dimensions of Case 1 (Rotation 0°, Twist 0°).

2 Numerical modelling

The aerodynamic performance of the various wing-sail configurations is evaluated using an in-house 3D inviscid solver followed by a 2D viscous solver. In more detail, the flow field around the various geometries is initially computed using a 3D potential flow Boundary Elements Method (BEM). This solver can operate in two modes. The first mode assumes the case of a uniform apparent wind vertical velocity profile, i.e. of constant velocity magnitude and angle, independent of the vertical position. The second mode accounts for a vertical boundary layer wind profile. The solver incorporates calculations for the apparent wind twist (the change of the apparent wind angle between consecutive vertical positions on the geometry – see also Figure 4, left) that the wing encounters while sailing. In both modes the output from the 3D BEM solver that is used in the next steps is the downwash (incident) angle as a function of the vertical (spanwise) position in the wing. The effective wind angle (a modification of the apparent wind angle, i.e. the actual “felt” incidence angle by a section when downwash effects are accounted) is necessary in order to include in a similar fashion to lifting-line methods, the perturbing 3D effects of the geometry on the incoming flow towards the 2D horizontal sections. These wing-sections have been pre-evaluated (pressure distributions per inflow angle) using a 2D inviscid-viscous solver (“Foil2W” [2]), capable of handling cases of mild to full separation. These pre-calculations allow us to create a large database per wind angle of attack for all sections of the geometries. So, the effective inflow angle at each section is associated to the pre-calculated pressure data via interpolations. The pressure data are then converted to 3D excitations in a strip-wise sense (i.e. the treatment of a 3D body by accounting for 2D strips along its vertical dimension). The flowchart of the above process, with the 3D BEM effective angle of attack guiding the interpolations in the 2D sectional pressure data (pre-calculated via the 2D viscous solver) is presented in Figure 2. The results of this strip-wise approach are expected to differ from a direct 3D CFD analysis, that requires however several weeks in order to be completed. A comparison of the obtained results of the method with an established in-house 3D viscous CFD solver is presented in section 2.4.

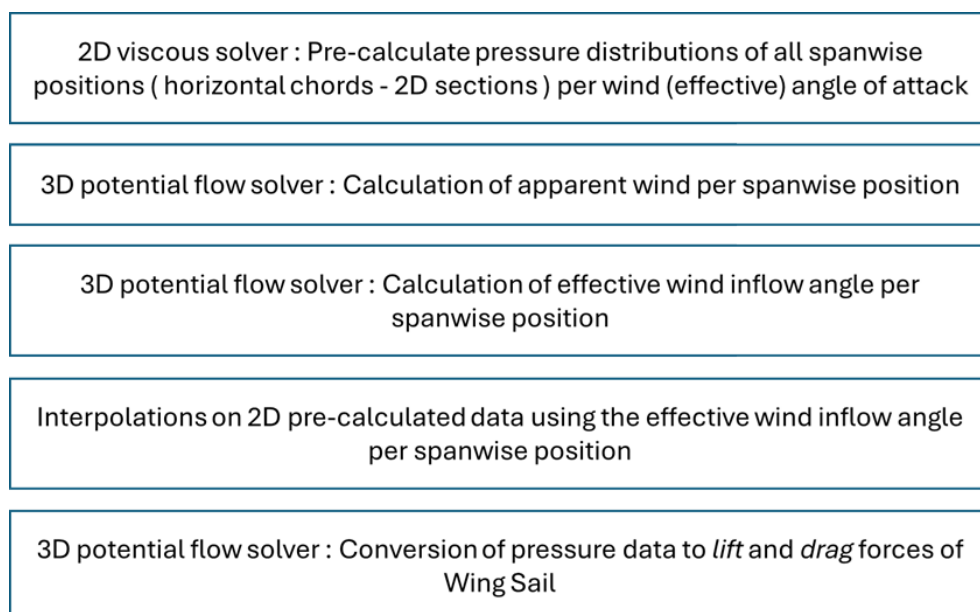


Figure 2: Flowchart of aerodynamics calculations process.

2.1 Calculation of apparent wind

In a strong resemblance to a yacht sail, the tested Wing-Sail configurations have a varying twist (Figure 3) as the sail is traversed upwards (spanwise). This design characteristic is necessary to exploit the occurring twist of the apparent wind velocity (Figure 4, left).

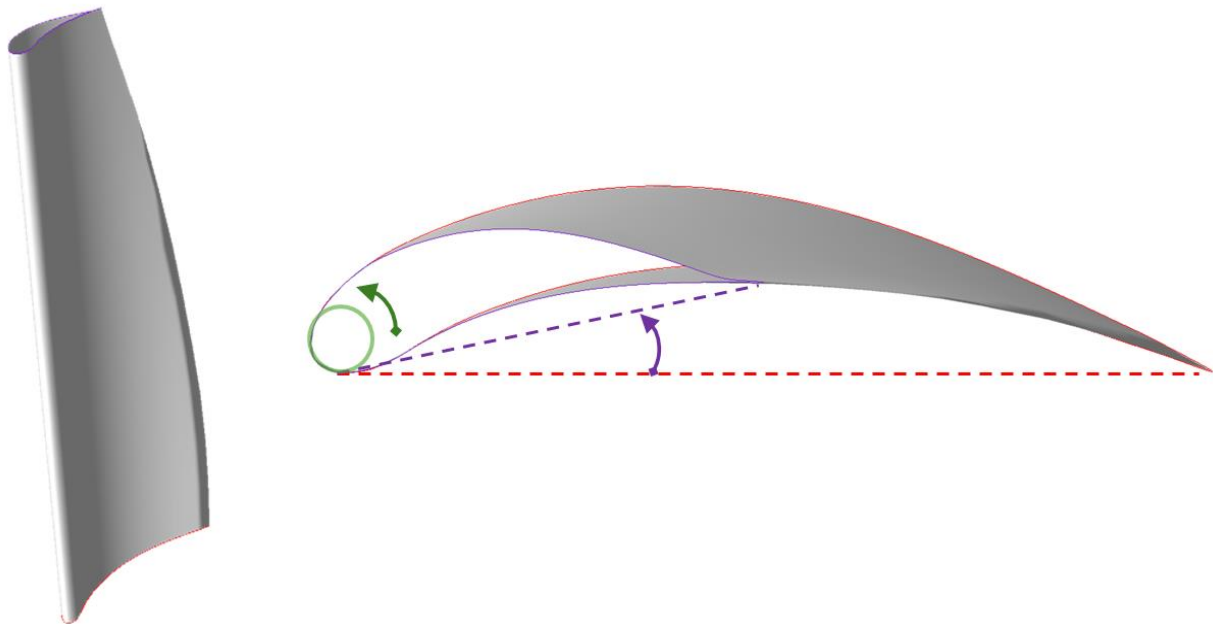


Figure 3: Root and tip chord sections, mast rotation (green arrow) and difference in twist (purple arrow).

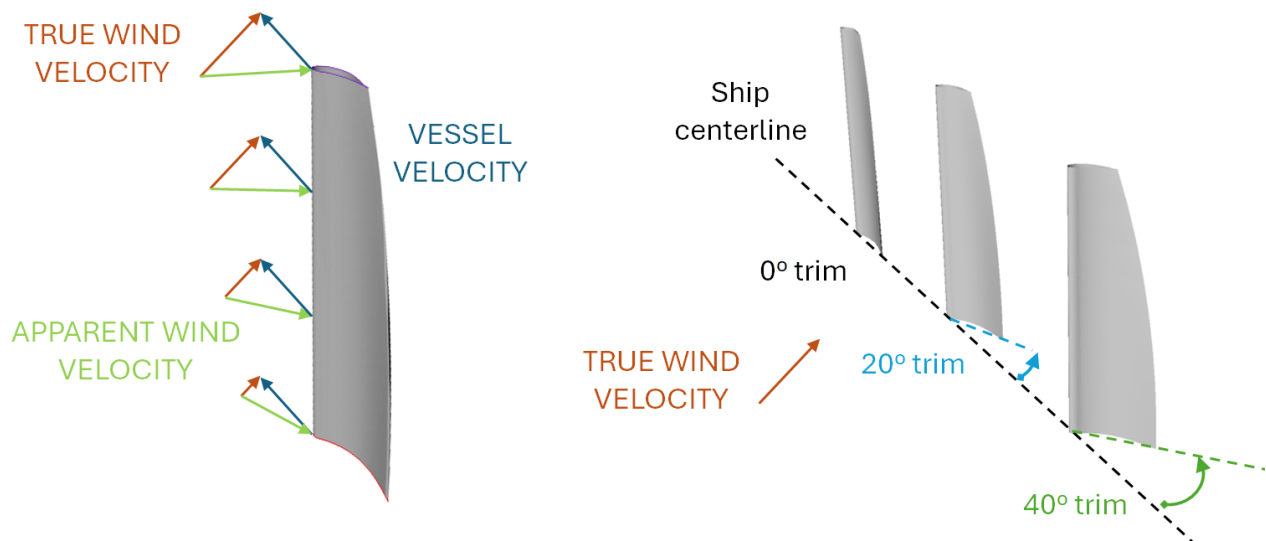


Figure 4: Apparent wind twist (left); Definition sketch of trim angle (random presented values of 0°, 20° and 40° trim) (right)

However, for terms of generality and in order to create the data that can populate the surrogate model of WP1, the lift and drag characteristics of the configurations and their vertical centre of effort as well, are presented under the assumption of uniform wind. In this case, the apparent wind velocity magnitude and angle are given from Equations (1) and (2). Note that the apparent wind angle is not necessarily the effective angle of attack for the wing sail. In fact, this is further affected by the downwash velocity, as shown in Figure 4 (left).

$$V_{AW} = \sqrt{V_{TW}^2 + V_B^2 + 2 V_{TW} V_B \cos a_{TW}} \quad \text{Eq. 1}$$

$$a_{AW} = \arccos\left(\frac{V_{TW} \cos a_{TW} + V_B}{V_{AW}}\right) \quad \text{Eq. 2}$$

As an example, Figure 5 shows contained calculations for a Wing Sail velocity (meaning the velocity along an axis that coincides with the wing chord) of $V_B = 6.5 \text{ m/s}$, a reference value of uniform true wind velocity equal to $V_{TW} = 10.0 \text{ m/s}$ and for a true wind angle between the two velocity vectors of $a_{TW} = 30^\circ$. The magnitude of the apparent wind velocity is calculated equal to $V_{AW} = 15.96 \text{ m/s}$ and the apparent wind angle is calculated equal to $a_{AW} = 18.2^\circ$. As this case regards uniform wind, the presented results are constant across all vertical positions (in the case of downwash and/or non-uniform wind this behavior changes).

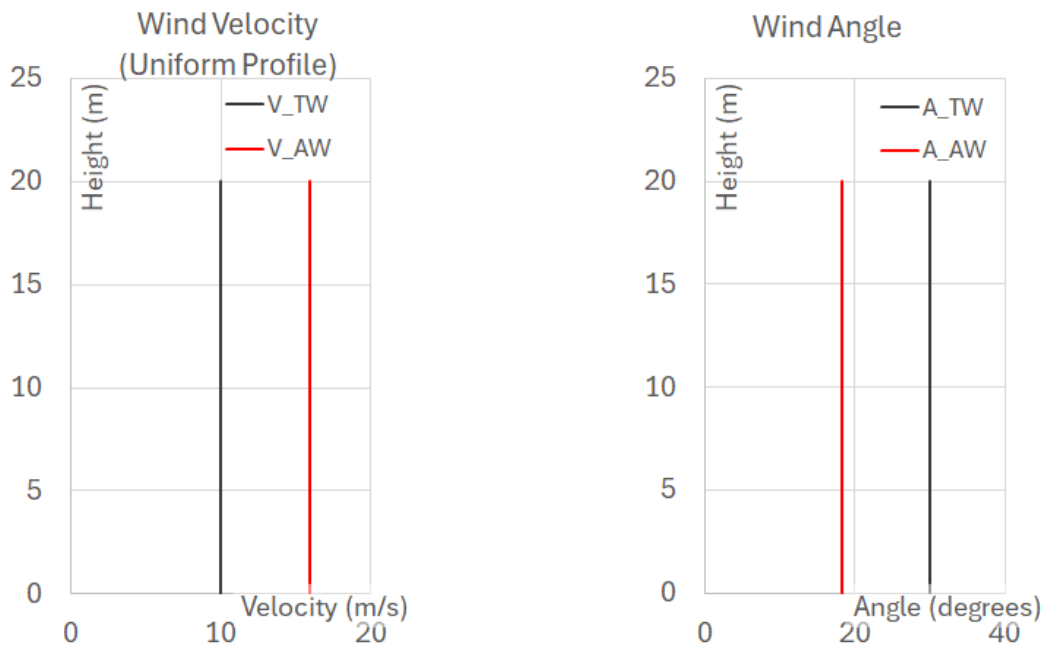


Figure 5: True and apparent wind velocity magnitude and angle. (Uniform true wind of 10.0 m/s, wing-sail velocity of 6.5 m/s, true wind angle of 30°. Occurring apparent wind velocity magnitude equal to 15.96 m/s and apparent wind angle equal to 18.2°)

In a second example, the calculations use the wind profile power law with a mean exponent value ($P = 0.11$ in Equation 3) approximating most weather conditions in open or closed seas and low reference heights [3], where u (m/s) is the wind velocity at an investigated height z (m), and u_r

and z_r are the reference values. The profile used in this study considered $u_r = 10 \text{ m/s}$ and $z_r = 15 \text{ m}$ respectively (Figure 6).

$$u = u_r (z/z_r)^P \quad \text{Eq. 3}$$

The apparent wind velocity magnitude and angle are given from Equations 1 and 2 and in Figure 6 some sample calculations for a Wing-Sail speed (velocity along its chord axis) of $V_B = 6.5 \text{ m/s}$ are shown, for a reference value of true wind velocity equal to $V_{TW} = u_r = 10 \text{ m/s}$ and a true wind angle of $a_{TW} = 30^\circ$.

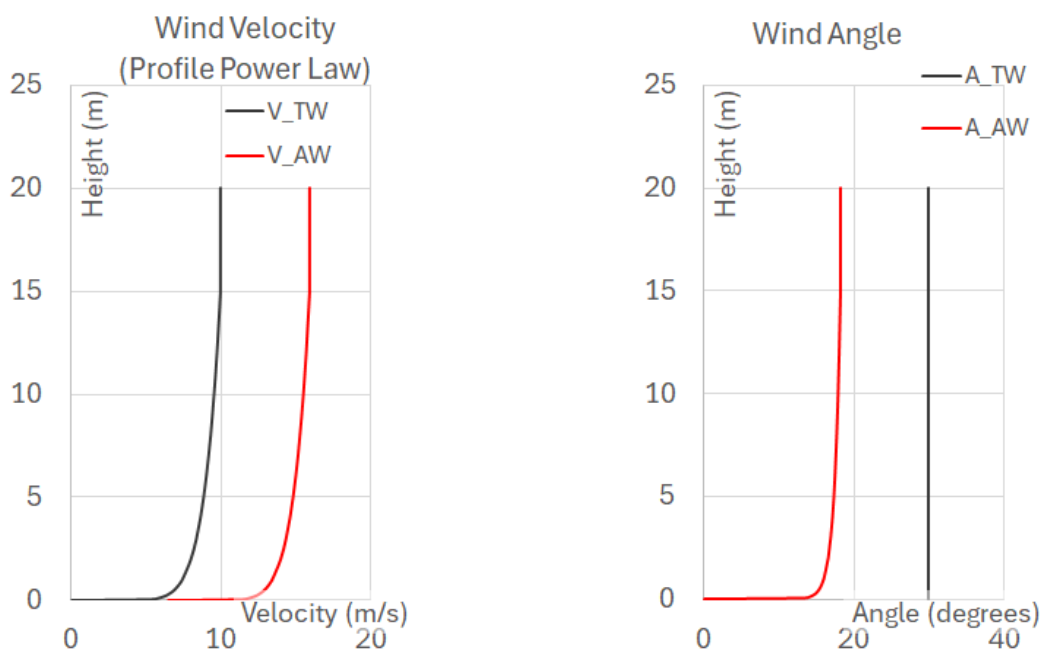


Figure 6: True and apparent wind velocity magnitude and angle. True wind dictated by Profile Power Law. (Reference true wind of 10.0 m/s at reference height of 15 m, wing-sail velocity of 6.5 m/s, true wind angle of 30° . Occurring apparent maximum wind velocity magnitude equal to 15.96 m/s and maximum apparent wind angle equal to 18.2°).

2.2 Potential flow BEM in 3D

This section contains the formulation of the 3D BEM potential flow model for the calculation of the effective wind inflow angle per spanwise position. The model utilizes a series of sources and dipoles distributions on the 3D surface of the wing, which is discretized to rectangular panels using cosine spacing at equal angular increments, spanwise and chordwise (Figure 7). In terms of the involved singularities the model is completed using a “frozen” wake surface, consisting solely of dipoles. The magnitude of the singularities, which initially is unknown, is obtained using the Dirichlet boundary condition for the potential on the body and the Kutta condition on the limiting trailing edge strip (Kutta strip). The formulation, which will be briefly presented below, is very similar to the formulations presented in Katz and Plotkin [4].

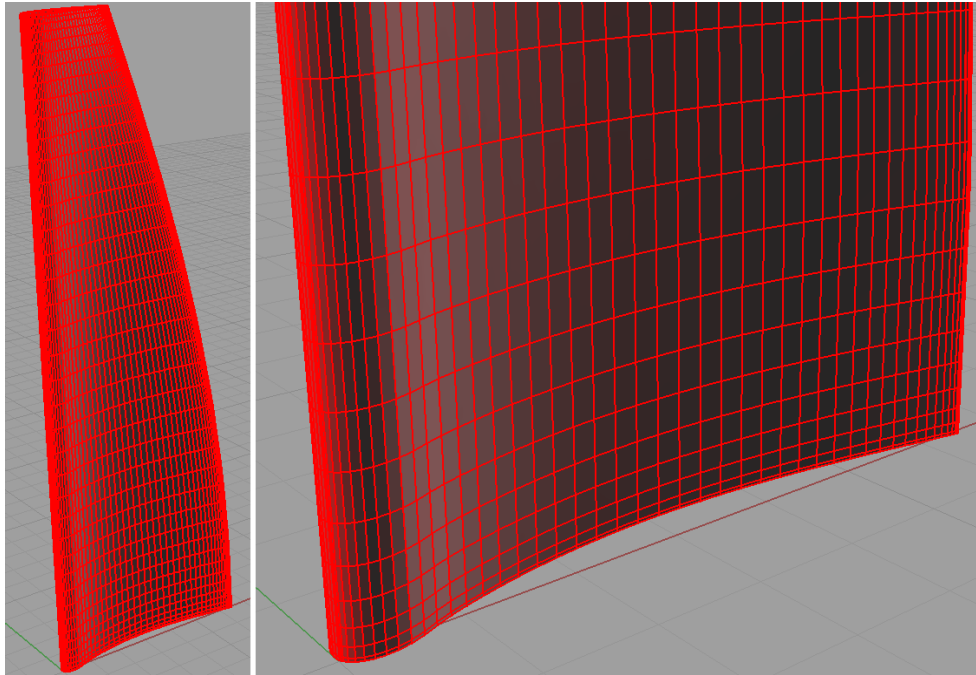


Figure 7: Discretized geometry with the cosine spacing scheme. Configuration no. 10.

Consider an inviscid, incompressible and irrotational and unbounded flow domain that can be characterized by a harmonic velocity potential function Φ (and \vec{V}). Then, by assuming a flow Φ_∞ (and $\vec{V}_\infty = \vec{V}_{AW}$) in the domain, any flow perturbations due to the presence of a solid body can be provided by an additional potential quantity Φ_P (and \vec{V}_P), associated with flow singularities of sources and dipoles (Equation 4). This quantity is added to the one that corresponds to the uniform flow, leading to total potential (Equation 5). The subscript “B” stands for the body geometry while “W” stands for the wake geometry.

$$\Phi_P(x, y, z) = \frac{1}{4\pi} \int_{B\&W} \mu \vec{n} \cdot \nabla \left(\frac{1}{r} \right) dS - \frac{1}{4\pi} \int_B \left(\sigma \left(\frac{1}{r} \right) \right) dS \quad \text{Eq. 4}$$

$$\Phi = \Phi_P + \Phi_\infty \quad \text{Eq. 5}$$

In Equation 4, r is the distance of the singularity from a point (x, y, z) in space, and \vec{n} is the normal vector pointing outside the body.

Obtaining the unknown magnitude of the singularities requires the enforcement of appropriate boundary conditions. We follow the Dirichlet conditions approach, by setting the total potential inside the body equal to a constant value (Equation 6) and by associating the source values to the discontinuity in the normal derivative in the velocity potential (leading to a form that appears similar to the Neumann boundary condition, Equation 7).

$$\Phi_i = \Phi_P + \Phi_\infty = \frac{1}{4\pi} \int_{B\&W} \mu \vec{n} \cdot \nabla \left(\frac{1}{r} \right) dS - \frac{1}{4\pi} \int_B \left(\sigma \left(\frac{1}{r} \right) \right) dS + \Phi_\infty = const \quad \text{Eq. 6}$$

$$\sigma = -\vec{n} \cdot \vec{V}_\infty \quad \text{Eq. 7}$$

The set of the boundary conditions is moreover appended by the steady Kutta condition at the trailing edge, associating the wake with the upper-side and lower-side trailing edge panels (Equation 8). Lastly, the set is completed with the radiation condition far away from the singularities (Equation 9). This is satisfied automatically due to the distance term in the denominator of the integral kernels.

$$\mu_W = \mu_U + \mu_L \quad \text{Eq. 8}$$

$$\lim_{r \rightarrow \infty} \nabla \Phi = 0 \quad \text{Eq. 9}$$

The above equations are transformed into a linear system of equations for the unknown values of σ and μ . The solution of the system allows for the calculation of the perturbation velocity (Equation 10) and the total velocity as well (Equation 11) on any point in the domain. From this point the downwash velocity and thus the effective wind angle can be calculated.

$$\vec{V}_P(x, y, z) = \nabla \Phi_P(x, y, z) = \frac{1}{4\pi} \int_{B\&W} \mu \nabla \left[\frac{\partial}{\partial n} \left(\frac{1}{r} \right) \right] dS - \frac{1}{4\pi} \int_B \sigma \nabla \left(\frac{1}{r} \right) dS \quad \text{Eq. 10}$$

$$\vec{V}(x, y, z) = \nabla \Phi(x, y, z) = \vec{V}_P + \vec{V}_\infty = \vec{V}_P + \vec{V}_{AW} \quad \text{Eq. 11}$$

The trailing edge panels, each of which hosts a dipole of constant strength, are equivalent to vortex rings ($\mu = \Gamma$). This makes the calculation of the downwash angle (ε_{z_1}) straightforward by invoking the contributions of the trailing vortex segments (Equation 12 for the inducing velocity of a single vortex segment). For any spanwise height position (e.g., z_1) then the downwash (w_{z_1}) is calculated as shown in Equations 13 - 15. In a continuation of the 2nd example that was presented earlier in section 2.1 and Figure 6 (for the apparent wind angle in the case of non-uniform wind and $V_{TW} = 10 \text{ m/s}$, $\alpha_{TW} = 30^\circ$, $V_B = 6.5 \text{ m/s}$) the effective angle (treated for downwash effects) for the no.10 configuration Wing-Sail is presented in Figure 8.

$$\vec{v} = \frac{\Gamma}{4\pi} \int \frac{d\vec{l} \times \vec{r}}{r^3} \quad \text{Eq. 12}$$

$$w_{z_1} = -\frac{1}{4\pi} \int \frac{\delta\Gamma}{z - z_1} dz \quad \text{Eq. 13}$$

$$\varepsilon_{z_1} = \frac{w_{z_1}}{V_\infty} \quad \text{Eq. 14}$$

$$a_{eff,z_1} = a_{AW,z_1} - \varepsilon_{z_1} \quad \text{Eq. 15}$$

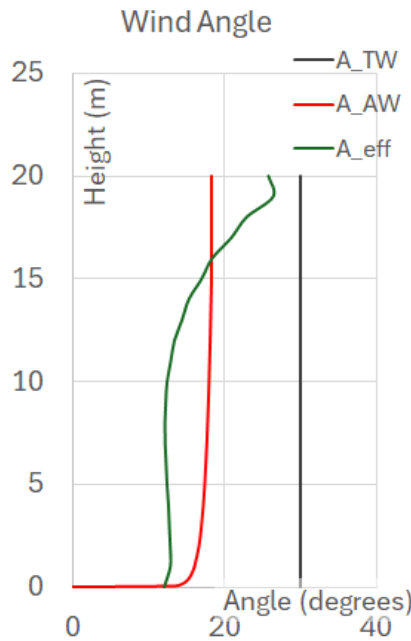


Figure 8: Wind angles (true, apparent, and effective). Configuration no. 10.

$$V_{TW} = 10 \text{ m/s}, a_{TW} = 30^\circ, V_B = 6.5 \text{ m/s}, a_{AW_ref} = 18.2^\circ.$$

2.3 Viscous flow in 2D and recreation of forces on wing surface

Each configuration is divided into nine horizontal 2D sections, spaced 2.5 meters apart (Figure 9).

These sections are evaluated aerodynamically from 0° to 90° in 5° increments using the in-house code Foil2W. This is a viscous-inviscid code where apart from the trailing edge wake, a boundary layer scheme is also used to identify the point of forward separation. The shed vorticities of the trailing edge and separated wakes are additionally defined by appropriate boundary conditions (Kutta, Kelvin) that close the inviscid (potential flow) model. More details are provided in [2]. Sample pressure coefficient distributions for the semi-span section ($z = 10 \text{ m}$) of configuration 10 are presented in Figure 10 in non-dimensional coordinates.

Having formulated the calculation for the effective wind angle at any sectional height, the 3D effects can be implicitly applied on the pre-calculated 2D pressure data (per wind angle) for the geometry sections. In detail, by assuming the velocity parameters of the wind and the Wing Sail (or in addition, of the vessel velocity) to be known we use the calculated effective angle of attack to retrieve the respective pressure coefficients from the pre-calculated data. For the cases where the effective

angles are in between the pre-calculated 5° increments, the pressure data are retrieved using linear interpolation. As the Wing Sail is discretized to rectangular panels that span all across the vertical extents of its geometry (the panel positions are not limited to the 9 horizontal sections - see also Figure 7) a second round of linear interpolations is then performed for each spanwise strip of panels for obtaining the respective pressure coefficient distributions.

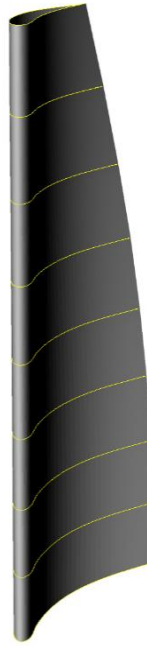


Figure 9: Equidistant (per 2.5 m) horizontal sections. Configuration no. 10.

The geometrical centre of each panel (i) is associated with its corresponding position of the pressure coefficient distribution (in non-dimensional x_i/chord position) and the retrieved value of the latter ($C_{P,i}$) is converted to a differential driving force ($\delta F x_i$) and side-force ($\delta F y_i$) using Equations 16 and 17 respectively. The calculations invoke the differential area of each panel (δS_i), its normal vector components (n_x, n_y) and the apparent wind velocity it experiences ($V_{AW,i}$).

$$\delta F x_i = C_{P,i} \frac{1}{2} \rho_{\text{Air}} V_{AW,i}^2 \delta S_i n_x \quad \text{Eq. 16}$$

$$\delta F y_i = C_{P,i} \frac{1}{2} \rho_{\text{Air}} V_{AW,i}^2 \delta S_i n_y \quad \text{Eq. 17}$$

The total forces on the wing, occurring from sum of the differential panel forces, are calculated as in Equations 18 and 19, while the non-dimensional driving and side force coefficients are calculated as in Equations 20 and 21.

$$F_X = \sum \delta F x_i \quad \text{Eq. 18}$$

$$F_Y = \sum \delta F y_i \quad \text{Eq. 19}$$

$$C_{F_X} = F_X / \left[\frac{1}{2} \rho_{\text{Air}} V_{\text{AW}}^2 S_{\text{Planform}} \right] \quad \text{Eq. 20}$$

$$C_{F_Y} = F_Y / \left[\frac{1}{2} \rho_{\text{Air}} V_{\text{AW}}^2 S_{\text{Planform}} \right] \quad \text{Eq. 21}$$

The reference values used for compute non-dimensional force coefficients are the velocity (i.e. at the reference height) of the apparent wind and the planform area of the wing sail (mean camber surface), i.e. the equivalent curved mid-surface between the pressure and suction sides. This can be retrieved with very good accuracy by summing panel areas of both pressure and suction sides and dividing by 2 (Equation 22).

$$S_{\text{Planform}} = 0.5 * \sum \delta S_i \quad \text{Eq. 22}$$

Finally, the lift and drag coefficients are computed as shown in Equations 23 and 24, where the reference apparent wind angle (a_{AW}) is used. In general, for inflow (apparent) angles of attack greater than $55^\circ - 60^\circ$ a full separation occurs.

$$C_L = C_{F_Y} \cos a_{\text{AW}} + C_{F_X} \sin a_{\text{AW}} \quad \text{Eq. 23}$$

$$C_D = -C_{F_X} \cos a_{\text{AW}} + C_{F_Y} \sin a_{\text{AW}} \quad \text{Eq. 24}$$

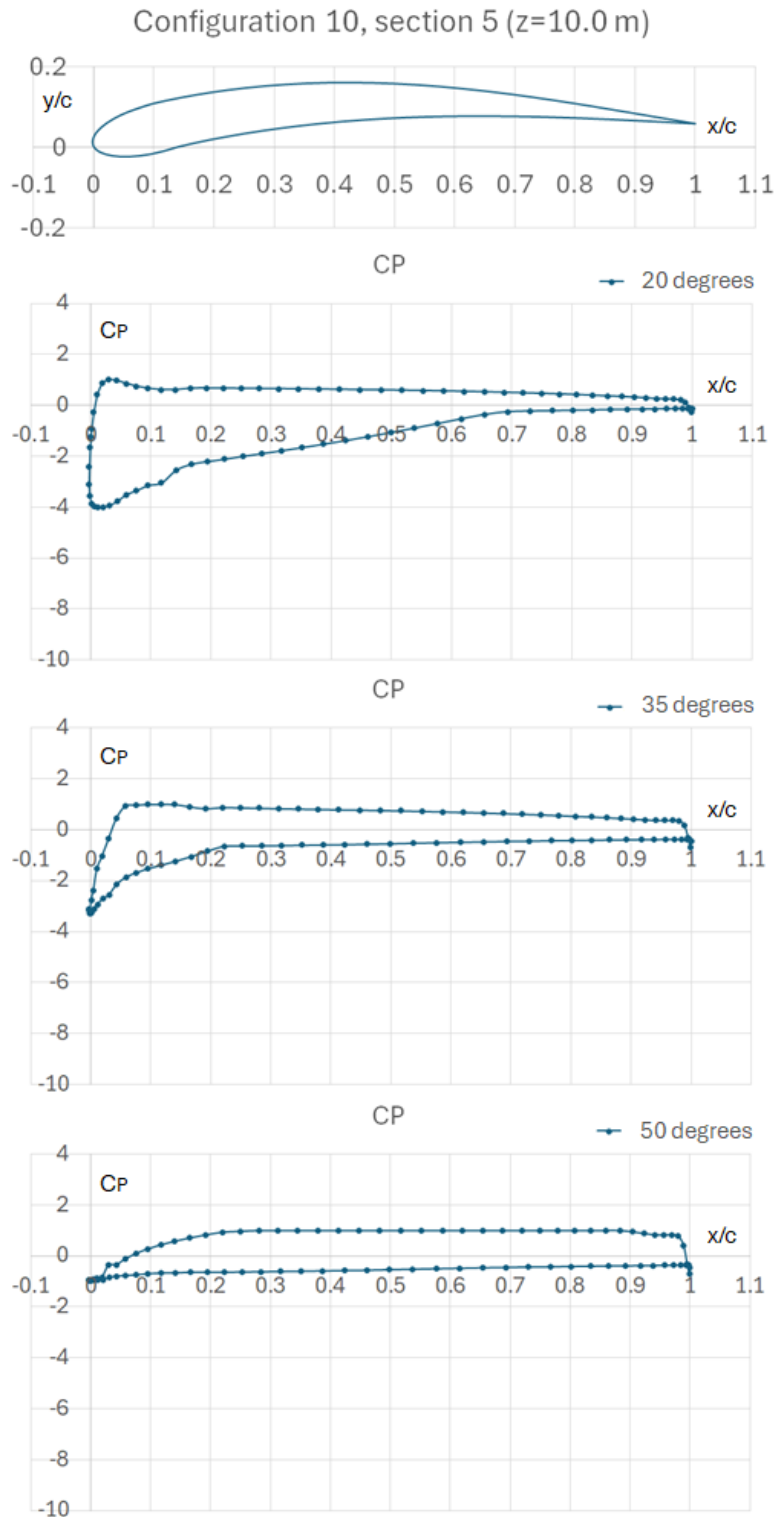


Figure 10: Configuration no. 10. Section 5 ($z = 10.0$ m). Sample pressure distributions. At 20° incidence separation near the trailing edge appears (horizontal curve beyond $x/c=0.7$), at 35° incidence the separation point has moved forward (horizontal curve beyond $x/c=0.2$), while at 50° incidence full leading edge separation has occurred.

2.4 Sample results: uniform vs. boundary layer profile wind inflow

2.4.1 Uniform wind flow

The lift and drag coefficients for the wing-sail configuration no. 22 with uniform wind are presented in Figure 11. The resolution of the sampling is per 0.5 degrees, intended for creating a database to populate the surrogate model of WP1. Representative values (per 5°) from the same dataset are contained in Table 2, along with data for the vertical centre of effort. Similar figures for the derived coefficients and the Vertical Centre of Effort (VCE) of the configurations, calculated with uniform wind are reported in Appendix A¹.

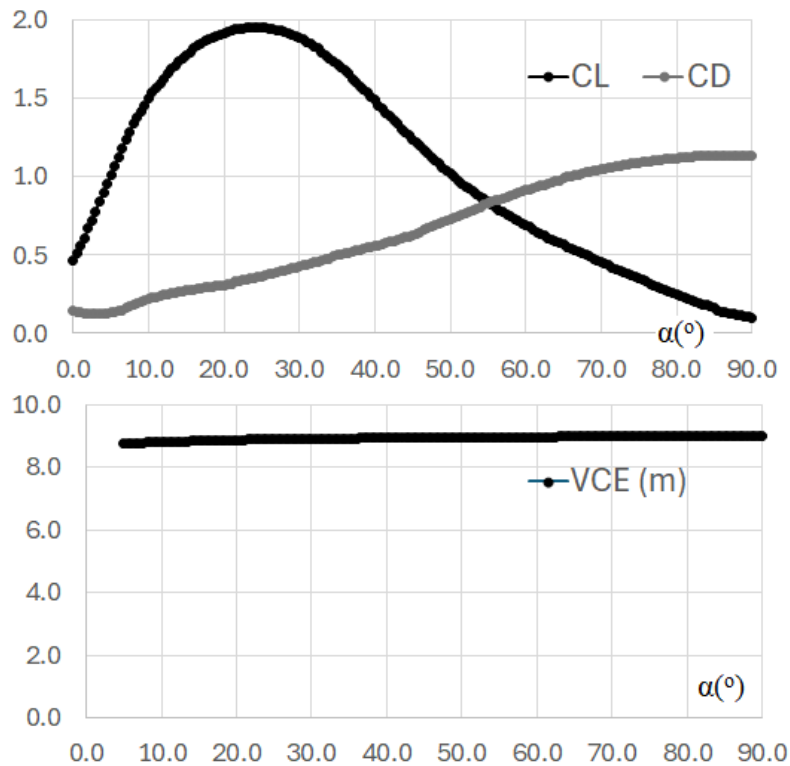


Figure 11: Force coefficients for wing-wail configuration 22.

Table 2: Force coefficients for wing-eail configuration 22.

Wind Angle (degrees)	C_L	C_D	Vertical centre of effort (VCE) (m)
0	0.470	0.150	8.320
5	1.010	0.140	8.750
10	1.500	0.220	8.820
15	1.780	0.280	8.850
20	1.920	0.310	8.880
25	1.960	0.360	8.900
30	1.890	0.430	8.920
35	1.720	0.500	8.930

¹ The corresponding data are available in .txt and .xlsx files in order to feed the tool developed in WP1.

40	1.490	0.560	8.940
45	1.240	0.630	8.950
50	1.020	0.730	8.960
55	0.840	0.830	8.970
60	0.690	0.920	8.980
65	0.570	0.990	8.990
70	0.460	1.050	9.000
75	0.350	1.090	9.000
80	0.250	1.120	9.010
85	0.160	1.140	9.010
90	0.100	1.140	9.020

2.4.2 Boundary layer profile

In real operational conditions the wind will be characterized by a boundary layer velocity (vertical) profile and the wing-sail device will be set to a specific trim (see also Figure 4, right) with respect to the incoming wind angle. Consequently, there are numerous possible profiles and trim settings, as well as many combinations of these parameters, making an a priori examination and analysis of every possible scenario computationally infeasible. For representative reasons however, we present herein a scenario in between, i.e., where we account for the vertical profile of the wind and we assume a zero trim of the device (with respect to the longitudinal axis of the ship). Considering thus the configuration no. 22 and the true wind velocity profile being characterized by a power law ($V_{TW} = u_r = 10 \text{ m/s}$, $z_r = 15 \text{ m}$), then the derived lift and drag coefficients are presented in Figure 12. The maximum lift value is compared to the case of uniform flow is reduced (about 12.85%) and the corresponding angle of maximum lift is transversed to the right (by 4°). A similar reduction trend is also observed for the drag values (Figure 12) with a reduction percentage (12.9%) for large inflow angles.

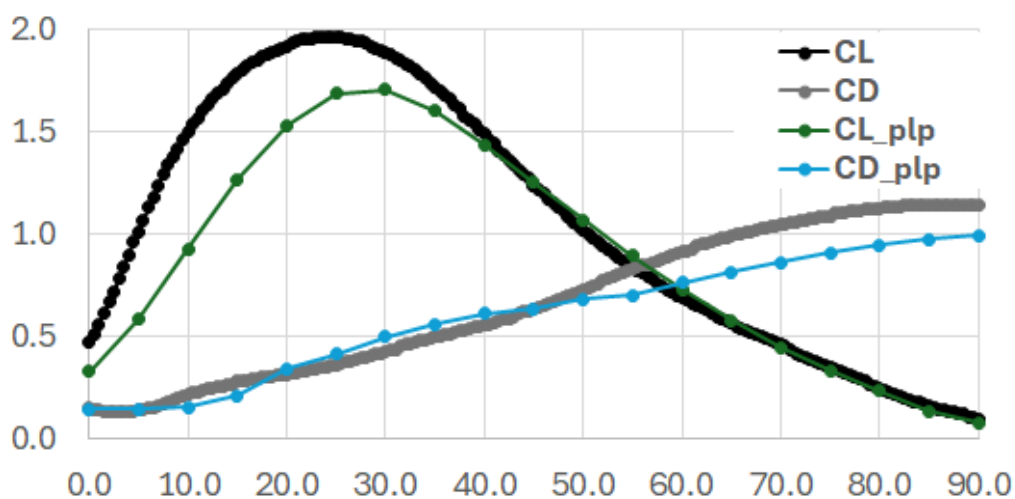


Figure 12: Force coefficients for wing-sail configuration 22. Uniform and power-law profiles.

As a verification of the method, Figure 13 presents the lift and drag coefficient values under uniform flow for configuration 22, calculated using MaPFlow, an in-house 3D CFD viscous solver. MaPFlow is an MPI parallelized unsteady Reynolds-Averaged Navier Stokes (URANS) solver, primarily

developed at the NTUA, for compressible flows and incompressible flows and offering several turbulence models of lower or higher fidelity [5], [6], and [7].

Although it is of high accuracy, the computational time it demands for the resolution of only 10 wind inflow angles, is in the range of several weeks. This limited its use for evaluating all configurations and fine angle resolutions, and made it necessary to develop a coupled solver like the one presented here.

The computations in MaPFlow that are presented in Figure 13 were performed using the two-equation $k-\omega$ SST Reynolds Averaged Navier Stokes Equation (RANSE) model for resolving a fully turbulent flow with a Reynolds number of approximately $Re=6 \cdot 10^6$. The differences in the presented results are expected, as the method introduced in this report is a potential flow method with viscous corrections for flow separation and operates in a strip-wise 3D sense (i.e, with the 3D effects introduced via the effective wind angle calculations), whereas MaPFlow is a fully 3D. The advantage of the presented method, however, is its faster computational time, especially when dealing with numerous configurations and high-resolution angle sampling, making it feasible to populate data tables for use in segregated surrogate solvers.

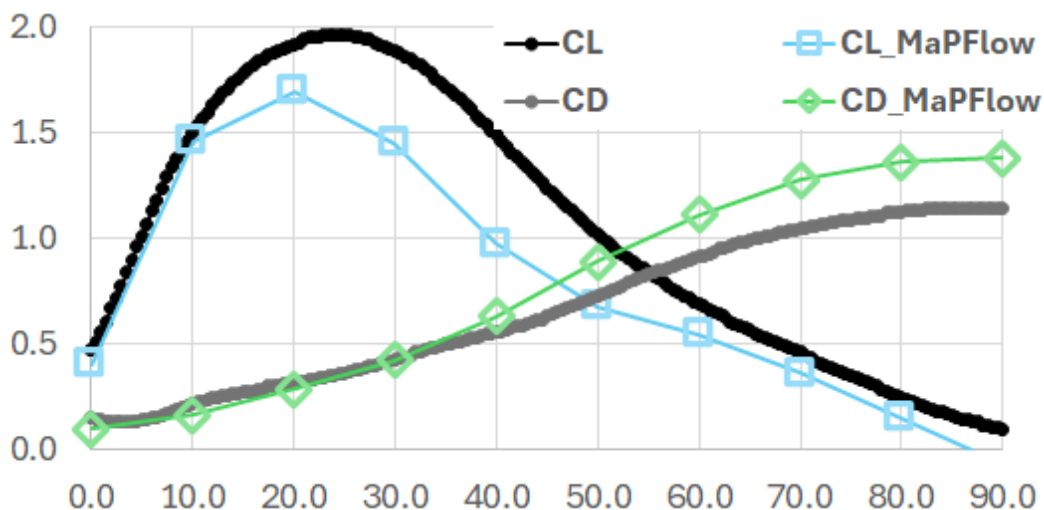


Figure 13: Force coefficients for wing-sail configuration 22. Uniform flow. Coupled solver and MaPFlow.

3 Closing remarks

In the present report a coupled model of potential and viscous solver is used to evaluate 28 configurations of the Wing Sail WASP system designed by AWS. This is a stowable and containerised device that can be placed on a vessel's deck in various numbers and positions. It can be adapted to different geometrical configurations by modifying its geometric parameters, such as rotation and twist.

The numerical model can account for either a uniform incoming wind flow or a boundary layer profile. Moreover, it can account for the velocity of the moving Wing Sail (apparent wind). The 3D flow effects are incorporated into the potential flow model using a BEM solver, which calculates the downwash velocity. Flow separation effects are provided by a 2D inviscid-viscous solver in terms of pre-calculated data for the distributions of the pressure coefficient at different wing sections. The effective angle of attack is calculated by relating the apparent wind and the downwash velocity is used in order to retrieve the necessary data from the pre-calculated pressure distributions. The latter are then converted to lift and drag forces and are made dimensionless for a comparative analysis. The coupled solver is able to reflect the geometric differences between the configurations, in the differences between the calculated force coefficients. The configurations are mostly efficient (high lift to drag ratios) in the range up to 40 degrees. Beyond that threshold, flow separation becomes dominant in most of the cases and performance is expected to be reduced.

The force coefficients can be used to assess the developing driving force (thrust) and side force of a vessel that is equipped with Wing Sail devices on board. With respect to the encountered wind conditions, the operator's goal would be to choose from among the different configurations and set an appropriate trim of the device, in order to maximize the offered driving force (additional thrust). Simultaneously there will be an unavoidable side force developing, the magnitude of which should be retained to reasonable levels by the operator. The reason for limiting this side-force is that it causes the ship to adopt a drift angle and a heel angle. Consequently, it induces an increase in the resistance of the ship and may cause stability issues.

References

- [1] (retrieved from) <https://www.consilium.europa.eu/en/policies/fit-for-55/>
- [2] Riziotis, V.A., Voutsinas, S.G. (2008), Dynamic stall modelling on airfoils based on strong viscous–inviscid interaction coupling. *Int. J. Numer. Meth. Fluids*, 56: 185-208. <https://doi.org/10.1002/fld.1525>
- [3] Hsu, S.A., Meindl, E.A., & Gilhousen, D.B. (1994), Determining the power-law wind-profile exponent under near-neutral stability conditions at sea. *J. Appl. Meteorol.*, Vol. 33, pp. 757-765. [https://doi.org/10.1175/1520-0450\(1994\)033<0757:DTPLWP>2.0.CO;2](https://doi.org/10.1175/1520-0450(1994)033<0757:DTPLWP>2.0.CO;2)
- [4] Katz, J., Plotkin, A. (2001). *Low-Speed Aerodynamics*. UK: Cambridge University Press. <https://doi.org/10.1017/CBO9780511810329>
- [5] Papadakis, G. (2014). *Development of a hybrid compressible vortex particle method and application to external problems including helicopter flows*. NTUA, PhD Thesis, Athens.
- [6] Ntouras, D., Papadakis, G. (2020). A Coupled Artificial Compressibility Method for Free Surface Flows. *Journal of Marine Science and Engineering*, vol. 8, no. 8, p. 590. doi: 10.3390/jmse8080590.
- [7] Manolesos, M., Papadakis, G. (2021). Investigation of the three-dimensional flow past a flatback wind turbine airfoil at high angles of attack. *Physics of Fluids*, vol. 33, no. 8, Aug. doi: 10.1063/5.005582

Appendix A – Lift and Drag Coefficients and Vertical centre of effort for each configuration and uniform inflow angle

The data used for Figure 14 to Figure 41 are available in .txt and .xlsx files in order to feed the tool developed in WP1.

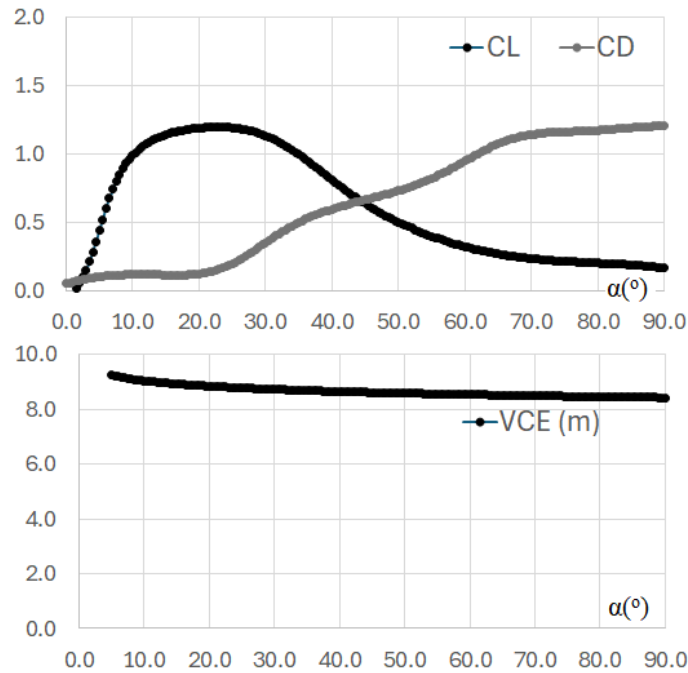


Figure 14: Force coefficients (top) and vertical center of effort (bottom). Configuration 1.

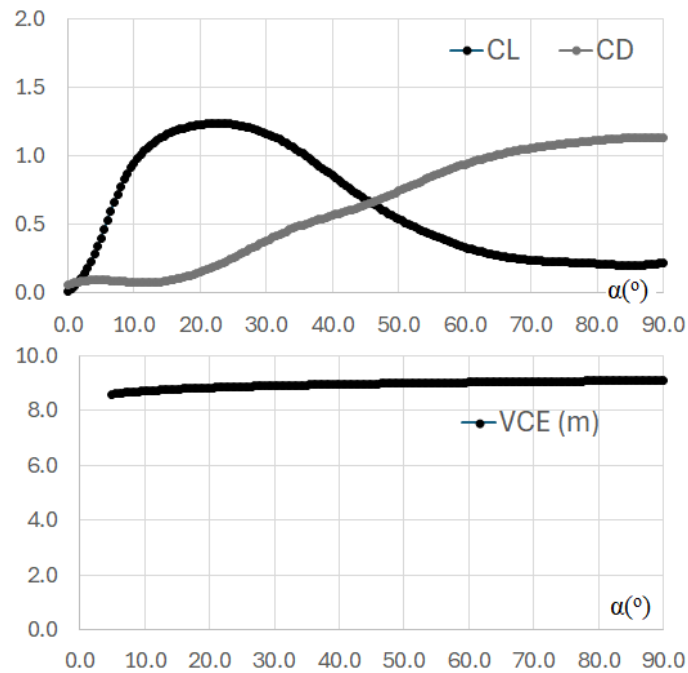


Figure 15: Force coefficients (top) and vertical center of effort (bottom). Configuration 2.

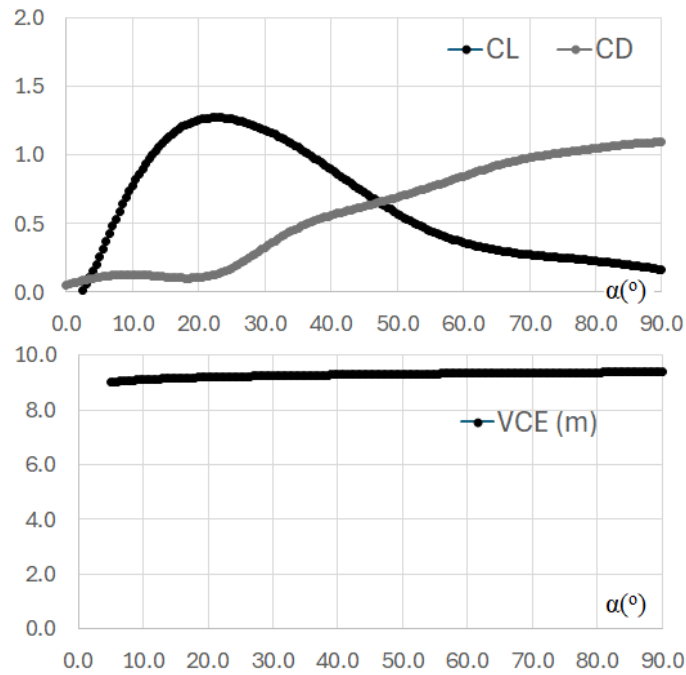


Figure 16: Force coefficients (top) and vertical center of effort (bottom). Configuration 3.

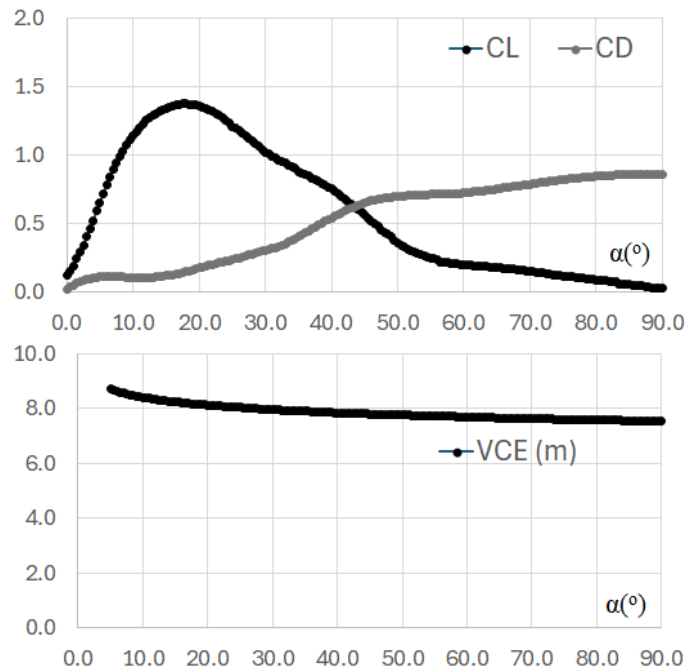


Figure 17: Force coefficients (top) and vertical center of effort (bottom). Configuration 4.

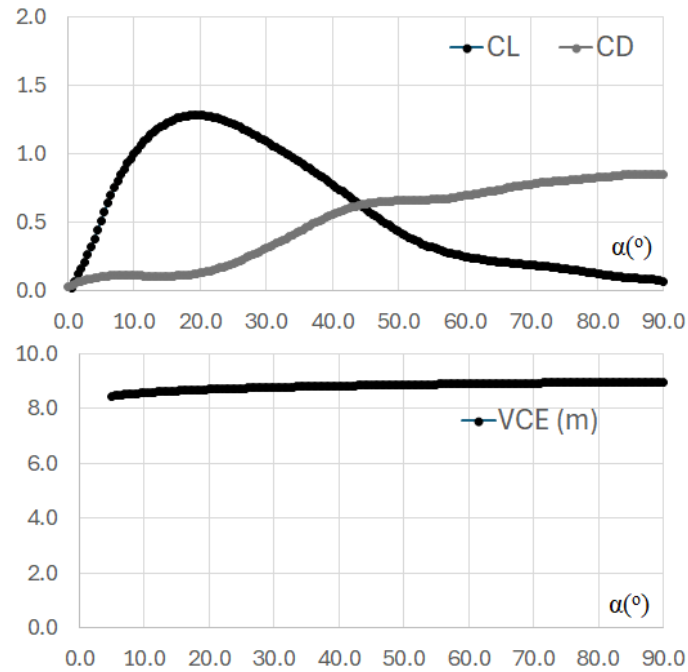


Figure 18: Force coefficients (top) and vertical center of effort (bottom). Configuration 5.

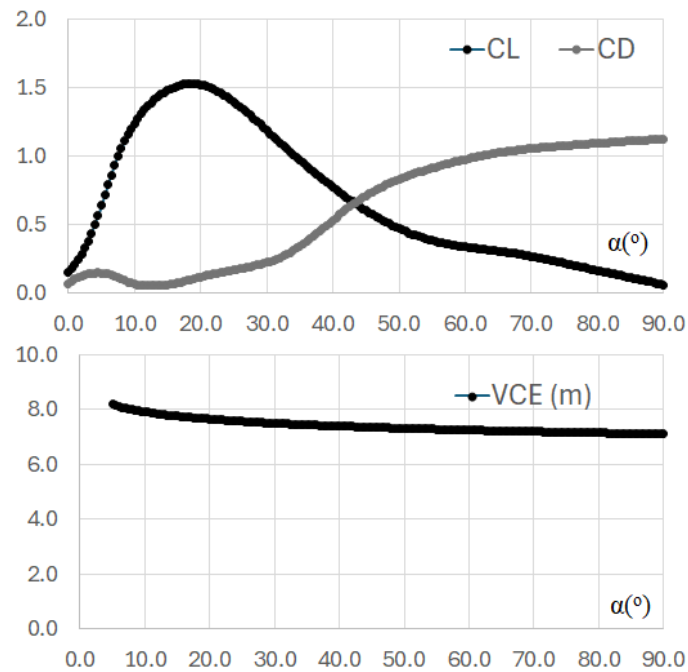


Figure 19: Force coefficients (top) and vertical center of effort (bottom). Configuration 6.

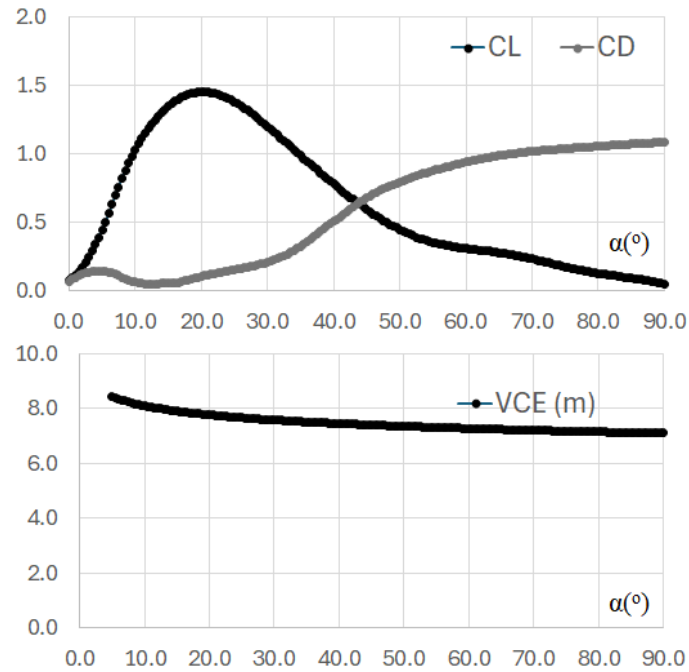


Figure 20: Force coefficients (top) and vertical center of effort (bottom). Configuration 7.

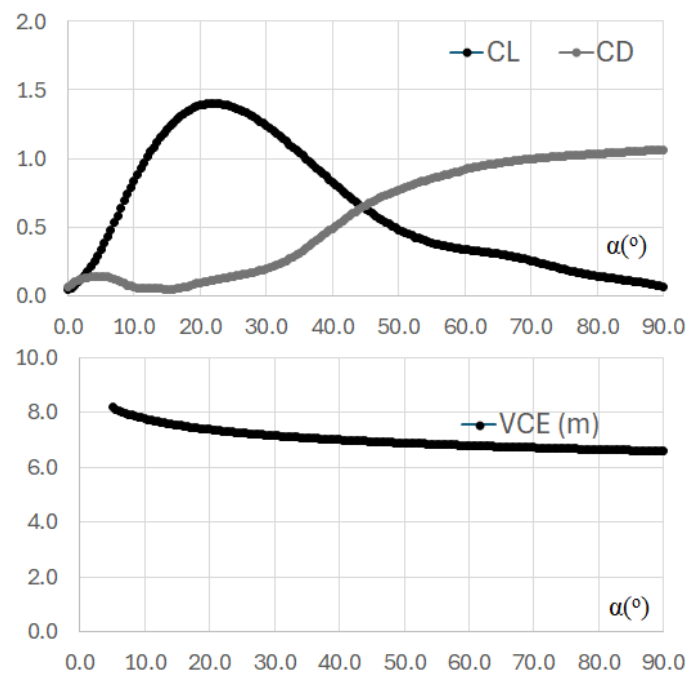


Figure 21: Force coefficients (top) and vertical center of effort (bottom). Configuration 8.

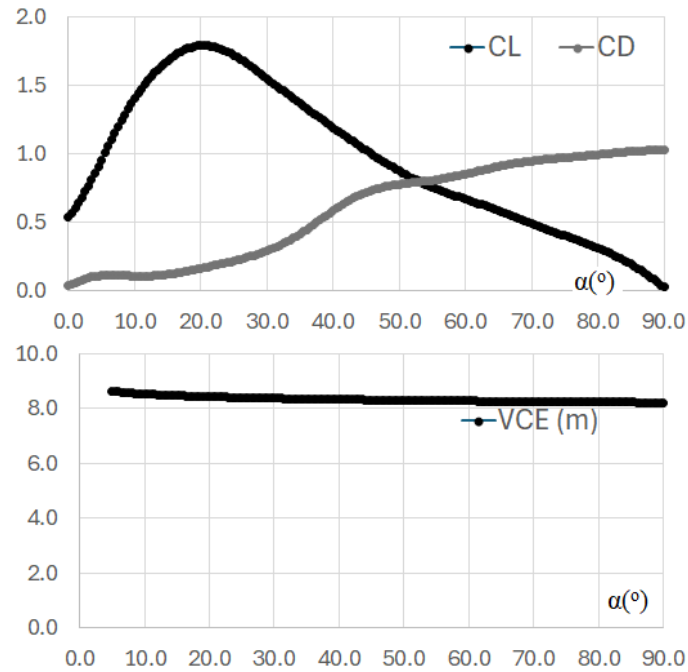


Figure 22: Force coefficients (top) and vertical center of effort (bottom). Configuration 9.

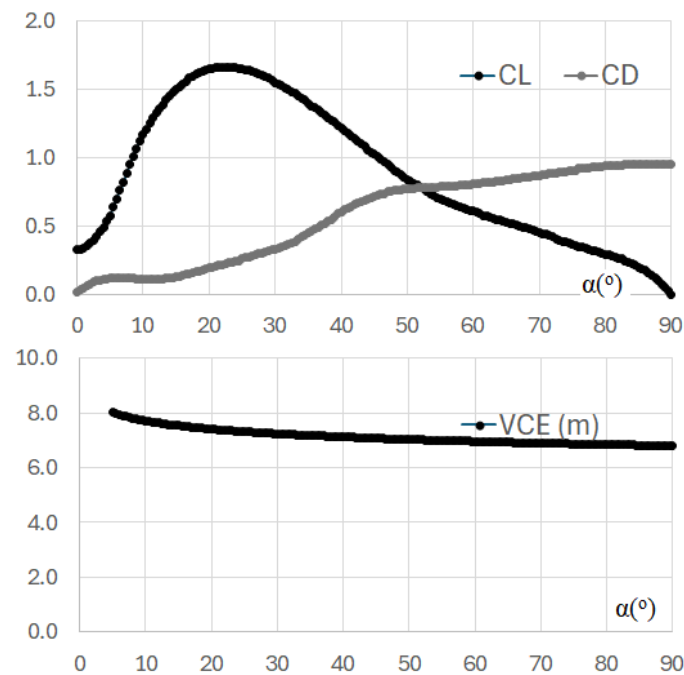


Figure 23: Force coefficients (top) and vertical center of effort (bottom). Configuration 10.

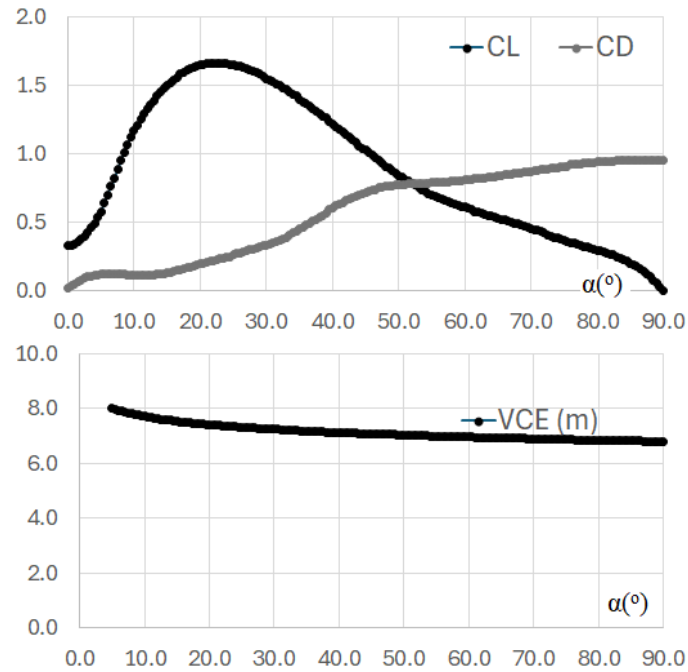


Figure 24: Force coefficients (top) and vertical center of effort (bottom). Configuration 11.

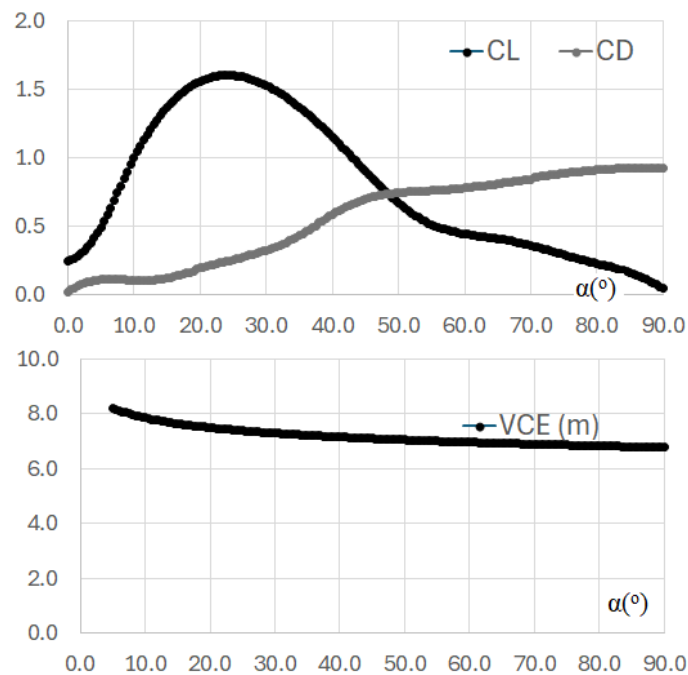


Figure 25: Force coefficients (top) and vertical center of effort (bottom). Configuration 12.

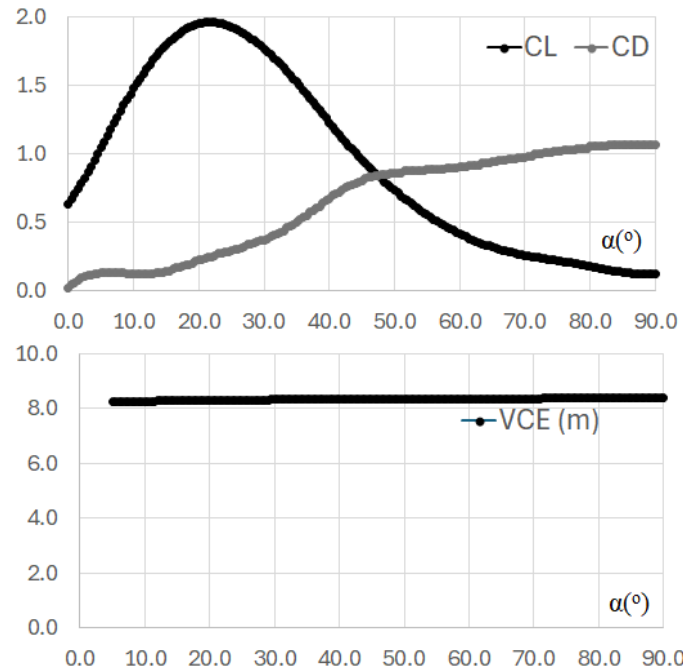


Figure 26: Force coefficients (top) and vertical center of effort (bottom). Configuration 13.

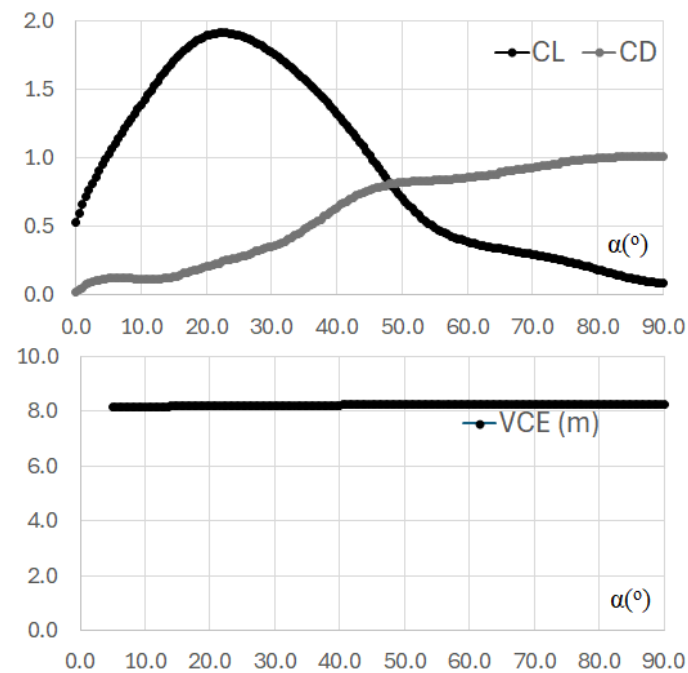


Figure 27: Force coefficients (top) and vertical center of effort (bottom). Configuration 14.

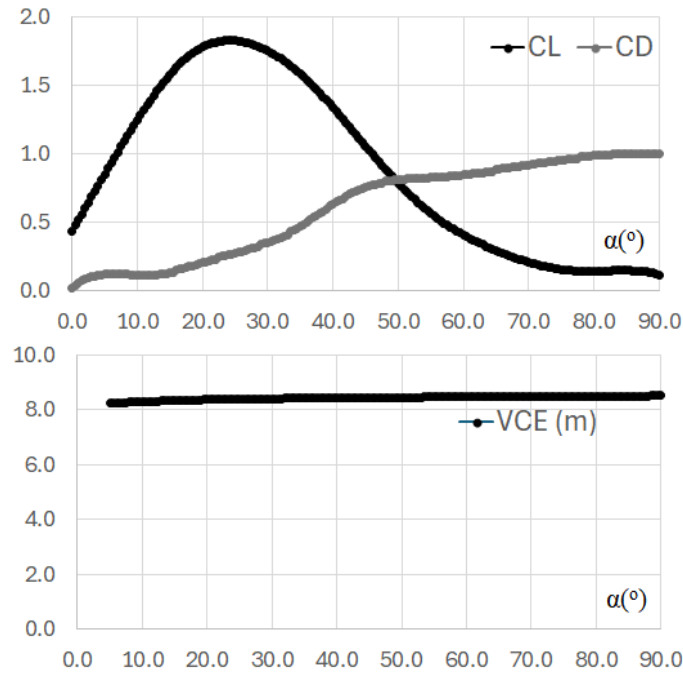


Figure 28: Force coefficients (top) and vertical center of effort (bottom). Configuration 15.

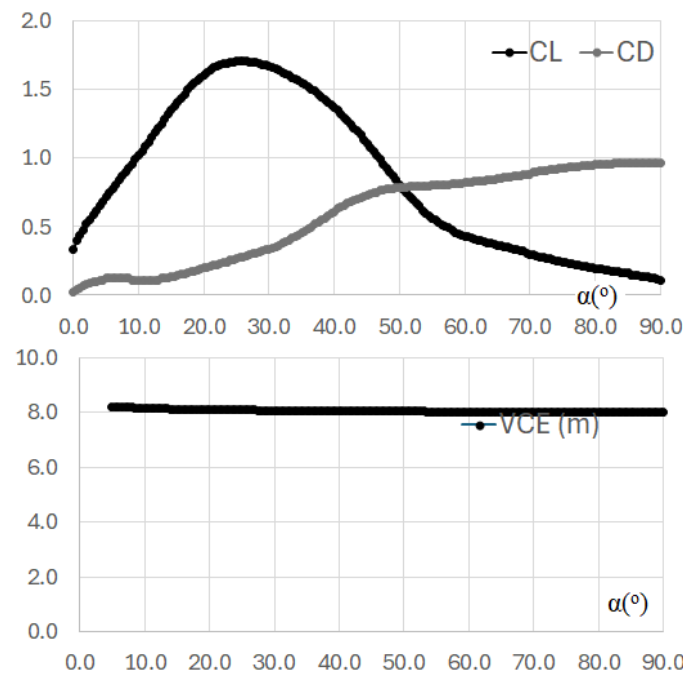


Figure 29: Force coefficients (top) and vertical center of effort (bottom). Configuration 16.

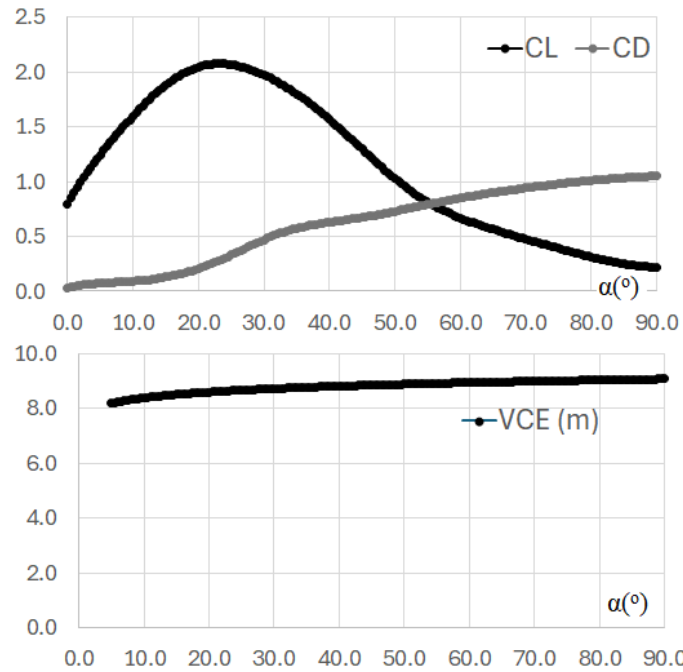


Figure 30: Force coefficients (top) and vertical center of effort (bottom). Configuration 17.

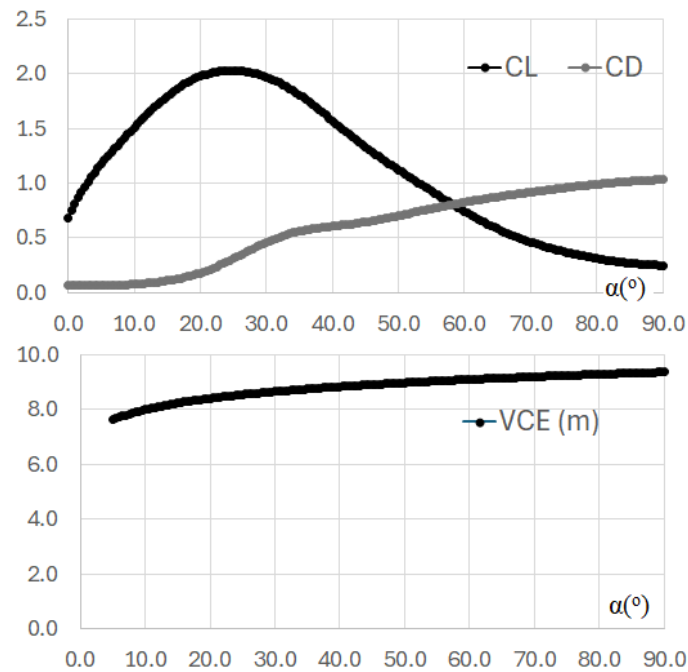


Figure 31: Force coefficients (top) and vertical center of effort (bottom). Configuration 18.

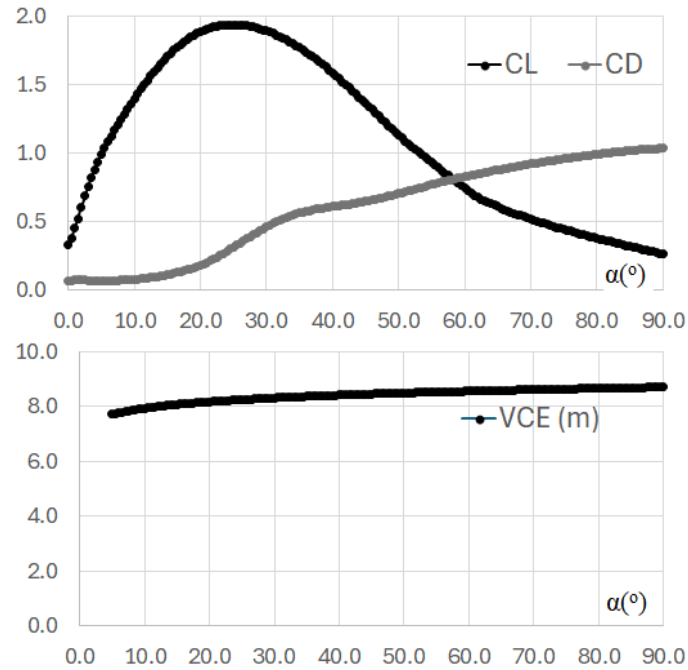


Figure 32: Force coefficients (top) and vertical center of effort (bottom). Configuration 19.

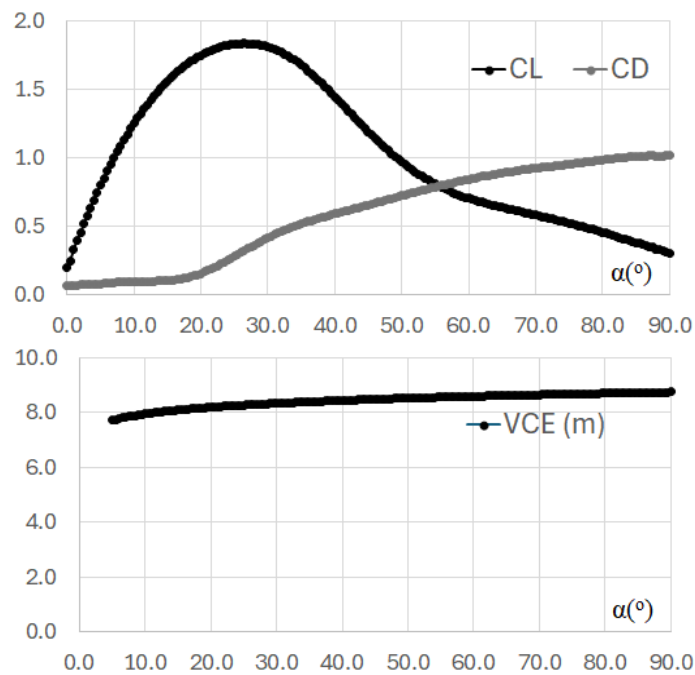


Figure 33: Force coefficients (top) and vertical center of effort (bottom). Configuration 20.

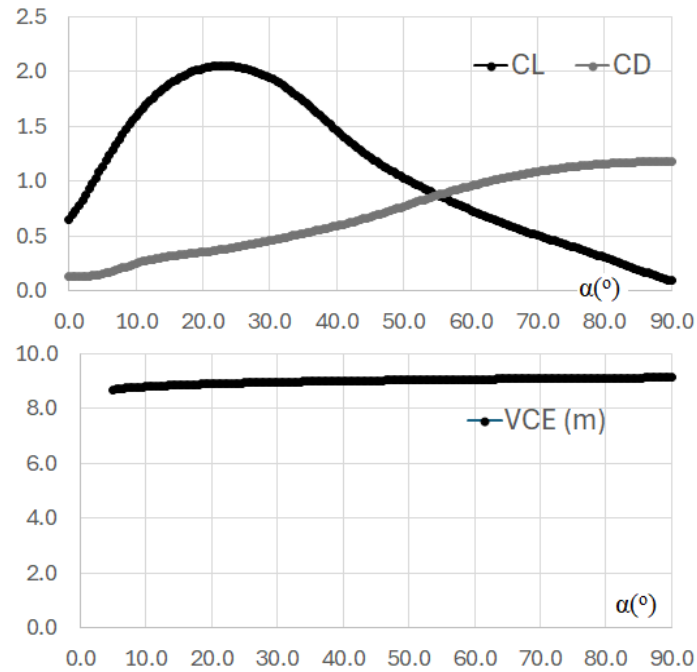


Figure 34: Force coefficients (top) and vertical center of effort (bottom). Configuration 21.

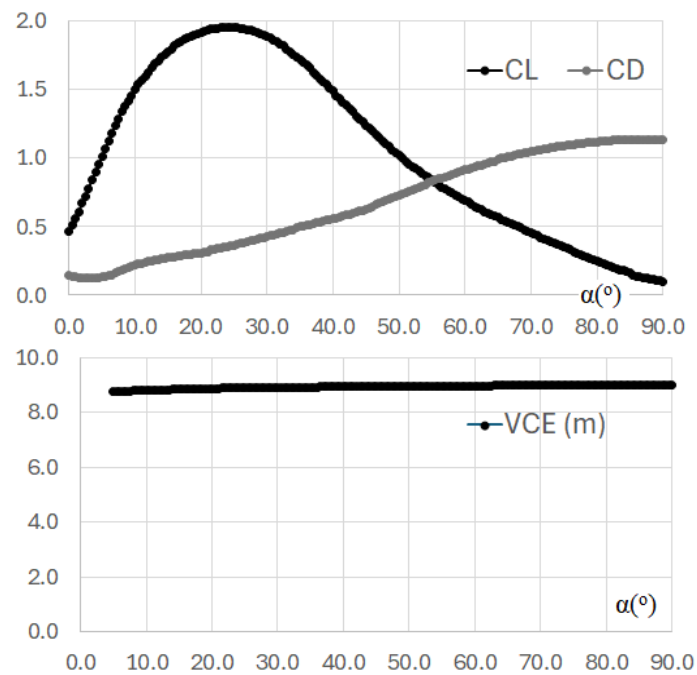


Figure 35: Force coefficients (top) and vertical center of effort (bottom). Configuration 22.

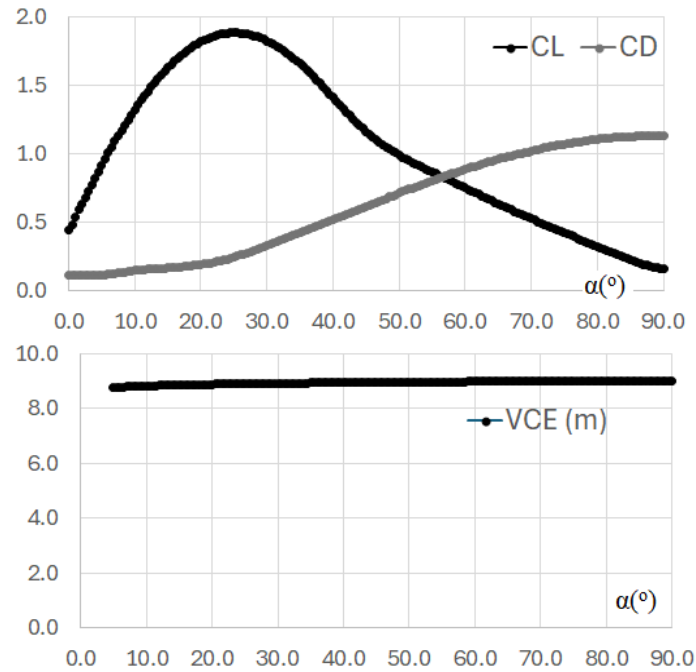


Figure 36: Force coefficients (top) and vertical center of effort (bottom). Configuration 23.

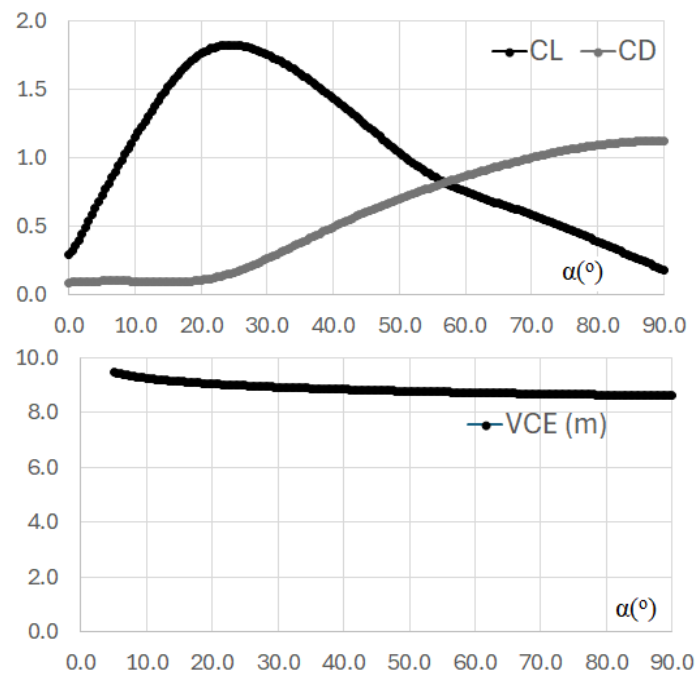


Figure 37: Force coefficients (top) and vertical center of effort (bottom). Configuration 24.

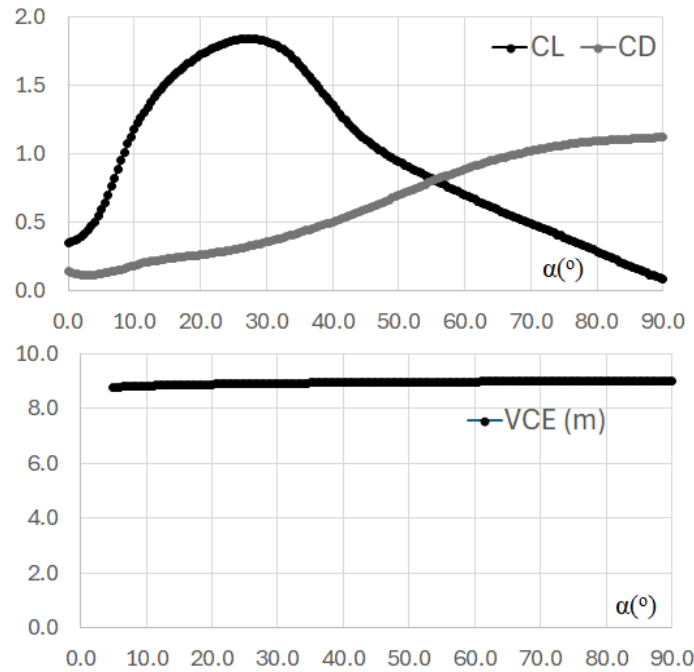


Figure 38: Force coefficients (top) and vertical center of effort (bottom). Configuration 25.

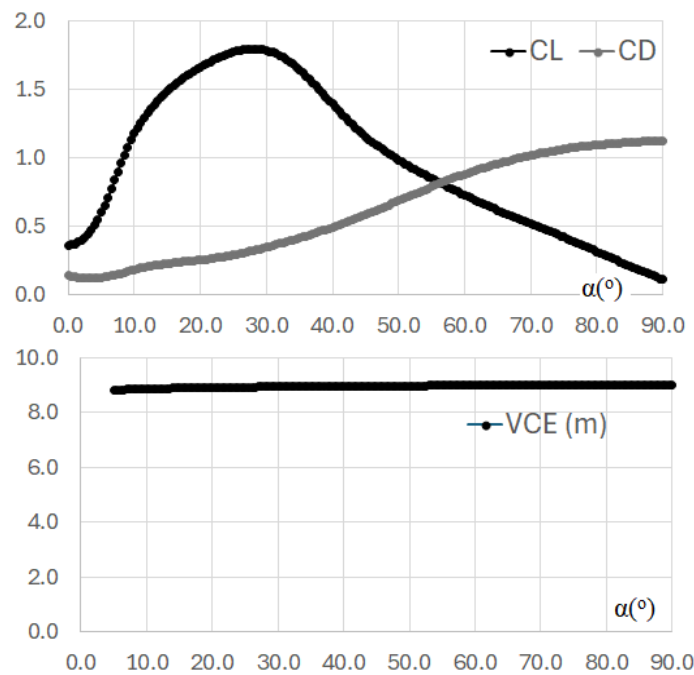


Figure 39: Force coefficients (top) and vertical center of effort (bottom). Configuration 26.

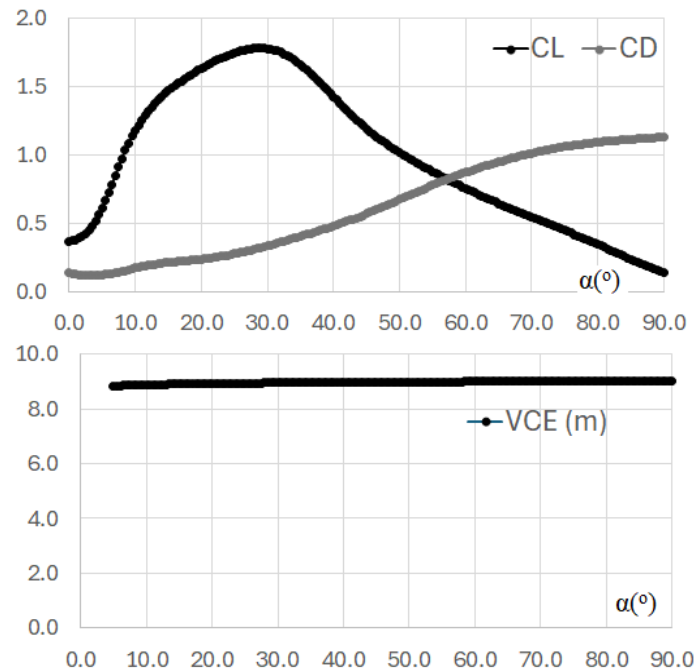


Figure 40: Force coefficients (top) and vertical center of effort (bottom). Configuration 27.

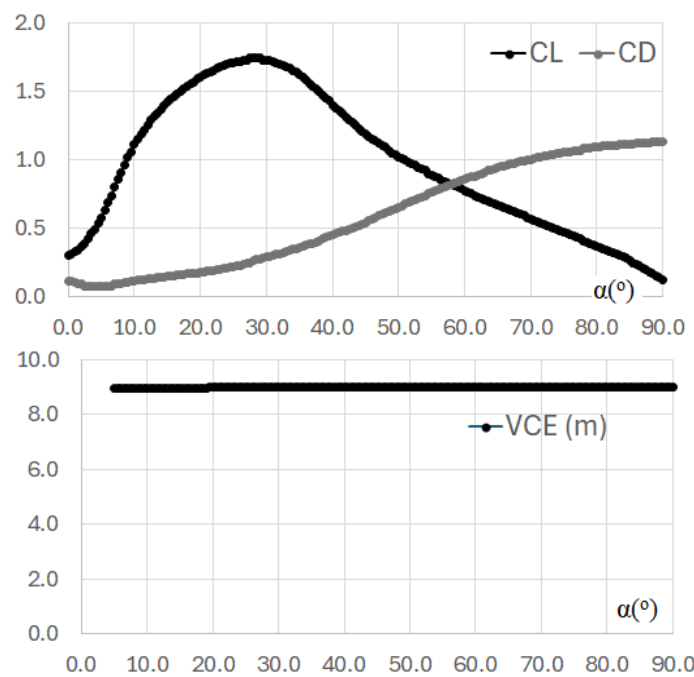


Figure 41: Force coefficients (top) and vertical center of effort (bottom). Configuration 28.